3D numerical modeling and experimental validation of diamagnetic levitated suspension in the static field

3D numerical modeling and experimental validation of diamagnetic levitating suspension in the static field

Giorgio De Pasquale *, Sonia Iamoni, Aurelio Som`a

Department of Mechanical and Aerospace Engineering, Politecnico di Torino, Corso Duca degli Abruzzi, 24–10129 Torino, Italy

A B S T R A C T

Diamagnetic levitation principle opens to promising solutions for innovative powerless and low stiffness suspension applicable to many technological fields. The peculiarities of diamagnetic suspen-sion make this design solution very attractive for some applications such as microdevices and energy harvesters. Low stiffness and powerless functioning are the most appreciable characteristics of this kind of suspension, despite their force–displacement curve is generally hard to predict and strongly nonlinear. The modeling complexity resides in the preliminary prediction of magnetic field distribution and in the calculation of diamagnetic forces as function of the levitation height. This work introduces a modeling approach for calculating the levitation height of a parameterized diamagnetic suspension composed of a ground of permanent magnets and a levitating mass made of pyrolytic graphite. The numerical discretization approach is used and the predicted values are compared with experiments providing good agreement between results.

1. Introduction

Magnetic levitation has been investigated as valuable design approach for the suspension of mechanical systems in various dimensional scales in alternative to the traditional elastic linear and nonlinear springs. Basically, the most relevant benefits provided by levitated suspension to the system dynamic response are due to their intrinsic low stiffness; additionally, their simple structure assures high reliability and long lifetime. More specifically, diamagnetic levitated suspension can operate without external power supply with significant advantages for the energetic efficiency improvement. Active magnetic levitation is typically applied to maglev transports and is operated through electromagnets; this solution, based on magnetic fields induced by the electric power supply, has its main drawback in the significant energy consumption. The alternative to active levita-tion is represented by passive levitated suspension, which can be divided in two typologies: the first type is based on the repulsive force between magnets and, usually, is simply composed by one permanent magnet attached to the frame and another one working as oscillating proof mass owing to the repulsive force. The polarity orientation of magnets allows generating the repulsive force between the facing sides; Mann and Sims [1] provide an example of this kind of levitated system. The second typology of levitated suspension, namely 'diamagnetic suspension', is based on the repulsive force generated inside diamagnetic materials. When surrounded by an external magnetic field, diamagnetic materials can generate a weak field that opposes the external one; if the configuration is properly studied, the magnetic repulsive force acting between the magnetic and the diamagnetic poles of the suspension may balance the gravity force and produce levitation [2,3]. Permanent magnets are generally used to gen-erate the external magnetic field; they are organized to form arrays or matrices of magnets and their polarity is properly oriented to maximize the diamagnetic force. Alternative strate-gies have been explored, for instance by using high-temperature superconductors to increase the levitation force [4] or with compact high field force magnets [5].

Traditional mechanical suspension systems are characterized by deformable elements that are able to store elastic potential energy when bended and then return almost the same amount of energy, except for small dissipations, when restoring the original shape; generally, their force–displacement characteristics are linear only for small travels and exhibit strong nonlinearities for long travels. The benefits of diamagnetic suspension compared to mechanical suspension are very significant, especially considering some applications (such as energy harvesting, inertial sensing, micromanipulation, bioengineering, etc.): their stiffness is some orders of magnitude lower, the energetic efficiency is comparable (but extremely higher than that of active magnetic suspension),

* Corresponding author. Tel.: +39 0110906912; fax: +39 0110906999.
E-mail addresses: giorgio.depasquale@polito.it (G. De Pasquale), sonia.iamoni@polito.it (S. Iamoni), aurelio.soma@polito.it (A. Som`a).

and their dimensions are sensitively smaller. The missing of deformable structural connections prevents some serious problems, such as the energy dissipation inside the material (e.g. thermoelastic damping), the energy dissipation with the surrounding fluid caused by viscous friction, and the mechanical fatigue effect, that reduces considerably the lifetime of mechanical parts when subjected to alternate loads [6].

Even though diamagnetism is a well-known physical property of materials and diamagnetic levitation has been deeply studied in the past [7–11], the application of this effect to practical devices and systems is still not mature. In the next years, the development of new fields such as micro- and nano-technology will offer the opportunity to exploit more in deep the properties of diamagnetic levitation and the benefits deriving from the integration of diamagnetic levitated components in real systems.

Several theoretical and empirical models of levitated systems have been described in the literature to explain and predict the static and dynamic behavior of the magnetic coupling associated to specific components with defined shape and dimensions. Simon et al. [12] discussed the equilibrium limits of a spinning rotor levitating on an annular magnet depending on its rotational velocity. The same authors in [13] found that the introduction of a diamagnetic material in some particular locations of magnet–magnet levitating systems allows stable equilibrium without external energy input, although this condition is generally prohibited by the Earnshaw theorem of levitation [7]. Cansiz and Hull [14] investigated the use of diamagnetic materials in magnetic bearings to study their characteristics in the static and in the dynamic behavior and their load-carrying capacity; in the paper is experimentally investigated a NdFeB disk-shaped rotor levitating over a ferrite magnet with a diamagnetic stabilizer in a vacuum chamber. The results show the rotational energy losses due to eddy currents and frequency of bearing rotation.

According to Earnshaw's theorem the equilibrium of forces acting on a ferromagnetic or paramagnetic body is not stable in a static magnetic field. A stable levitation can be achieved using a levitated body made of a magnetic material [15] having a relative permeability locally less than one; diamagnetic and superconducting materials can be used for this purpose. Diamagnetic materials present a value of magnetic permeability that differs only slightly from unity so with these materials the attained levitated load is very small compared to superconductors, which have practically zero permeability. Even though the levitation capacity is greater than that of the diamagnetic materials, the cooling cost, hysteresis and maintenance decrease the practical usefulness of superconductive bearings. This is the reason why the diamagnetic materials with no hysteresis can be used to create a stabilizer in the magnetic bearings if the application requires rather small loads.

Other studies investigated the dissipations occurring in diamagnetic suspension due to eddy currents [16]; this effect may have relevant influence on the suspension dynamics, in particular on its quality factor and on the response to impulsive excitations. Analytic compact models and numerical models based on the finite elements method (FEM) have been introduced to predict the static levitation height of the suspension starting from the magnetic field distribution and the discretization of the diamagnetic force induced in the levitating mass [18,19].

Also Chen et al. [17] investigated the eddy-current effect on the performance of diamagnetic bearings. Eddy current could be induced in the diamagnetic bearing with viscous forces opposing the relative motion between the rotor and the stator. Such damping mechanism was analyzed with a thin-sheet model and the image method and compared with that due to aerodynamic effects so as to give an idea of its significance at the microscale. The obtained results indicated that, due to its rotating nature, eddy current has a destabilizing effect on the diamagnetic bearing which is operated in the supercritical range, whereas for operation in the subcritical region, it provides a simple and effective damping mechanism.

Some examples of devices and prototypes with embedded magnetic levitating components were effectively described. The acceleration sensor introduced by Barrot et al. in [20] is based on a force-feedback sensing concept that exploits the optical detec-tion of a levitated inertial mass, providing high accuracy and sensitivity to the measurements. Instead, the accelerometer described by Garmire et al. in [21] is based on the micro electro-mechanical systems (MEMS) technology and includes a miniatur-ized proof mass made with a diamagnetic material that is suspended on a magnetic ground; the acceleration measurement is provided again by an optical detection of the mass motion. Sometimes, MEMS accelerometers include special finger-shaped features, namely 'comb drives', used to detect the mass motion via their capacitance variation; the electrostatic interactions between comb drives may induce the magnetic levitation of the structure, offering the opportunity to control its position in static and dynamic conditions thanks to this particular magnetic micro-suspension [22,23]. Li et al. [24] efficiently applied a magnetic levitated suspension system to an atomic force microscope for the calibration of the lateral force. A diamagnetic rotor suspension was developed in [25] and in [26] for optical devices positioning purposes.

Differently from the previous studies, this work does not focuses on a specific device but introduces a general modeling approach to predict the behavior of diamagnetically levitated suspension [27]. A very basic layout of the suspension is considered and the calculation predictions are supported by experimental validation tests. The behavioral prediction of simple structures and their characterization by experiments permit to setup the design parameters of more complicated solutions to suit every specific application. This statement led to consider the particular typology of samples used in this work, instead of more complicated specimens addressed to more specific fields of application. After the preliminary analysis of the theoretical background of magnetic levitation, the numerical discretization of the suspension is presented with the goal to predict its static properties, i.e. levitation height and stiffness. The diamagnetic force acting on the levitating part is calculated by means of the finite elements approach. The suspension is defined through the parameterization of its geometrical dimensions, according to the approach already used in the literature [19,28,29] in order to derive size-dependent properties of the suspension.

2. Theoretical background

This section reports the basic physical relations and interactions between the external magnetic field ($\vec{H}$) and diamagnetic materials. The magnetic behavior of diamagnetic materials depends on its orbital magnetization: when an external magnetic field influences a diamagnetic material, the electrons of its atoms react to the field by orbiting in such a way as to create an opposite magnetic field. The magnetization of an elementary volume ΔV of material is defined by the magnetic dipole per unit volume ($\vec{M}$) that is also called induced magnetization; for some materials such as permanent magnets, it persists even if the external magnetic field is removed.

In diamagnetic materials, $\vec{M}$ depends on the external magnetic field and on the magnetic susceptibility (χ) of the material. The magnetic susceptibility of anisotropic materials varies depending on the directions; for example, the pyrolytic graphite used in the

next part of the work for the experimental characterization of diamagnetic suspension has anisotropic properties.

The induced magnetization is related to the magnetic flux density ($\vec{B}$) by the equation

$$\vec{M} \cong \chi\left(\frac{\vec{B}}{\mu_0}\right) \tag{1}$$

where μ_0 is the magnetic permeability of vacuum ($4\pi \times 10^{-7}$ N/A^2) and the magnetic flux density, also known as induced magnetic field, is a vectorial quantity that can be linked to the external magnetic field using the following equation:

$$\vec{B} = \mu_0(1+\chi)\vec{H} = \mu_0\mu_r\vec{H} \tag{2}$$

$\mu_r = (1+\chi)$ is the relative magnetic permeability and $\mu = \mu_0\mu_r$ is the magnetic permeability; they are both dependent on the direction considered for anisotropic materials.

Thanks to their properties, diamagnetic materials are able to generate a weak opposite field when inserted into an external magnetic one; therefore, in particular conditions, the magnetic force acting on the diamagnetic mass may balance the gravity force and produce levitation.

Diamagnetic materials are characterized by very small negative χ (that means μ_r slightly smaller than 1). Exploiting this fact and their anisotropy, Eq. (1) can be rewritten as follows:

$$\vec{M} = \left(\frac{1}{\mu_0}\right)\cdot\left(\chi_x \cdot B_x \cdot \vec{i} + \chi_y \cdot B_y \cdot \vec{j} + \chi_z \cdot B_z \cdot \vec{k}\right) \tag{1a}$$

The total potential energy of a unit volume of diamagnetic material immersed in the field with magnetic flux density $\vec{B}$ is

$$W = -\left(\sum\nolimits_{\Delta V} \vec{M}_i\right)\cdot\vec{B} \tag{3}$$

and the elementary diamagnetic force acting on the unit volume can be calculated as

$$\vec{f}_m = -\nabla(W) = \nabla(\vec{M}\cdot\vec{B}) = \vec{M}\cdot\nabla(\vec{B}) \tag{4}$$

From the combination of Eqs. (1a) and (4), the expression of the force per unit volume becomes finally

$$\vec{f}_m = \frac{1}{2\cdot\mu_0}\cdot\nabla\left(\chi_x \cdot B^2{}_x + \chi_y \cdot B_y^2 + \chi_z \cdot B_z^2\right) \tag{5}$$

The total magnetic force acting on the diamagnetic proof mass can be obtained by integrating the unit force on the entire volume:

$$\vec{F}_m = \int_V \vec{f}_m \cdot dV \tag{6}$$

The vertical component of the magnetic force that opposes to the gravity one and produces levitation is given by

$$F_{m,z} = \int_V \frac{d(f_m)}{dz}\cdot dV = \int_V \frac{1}{2\mu_0}\frac{d(\chi_x B_x^2 + \chi_y B_y^2 + \chi_z B_z^2)}{dz}\cdot dV \tag{7}$$

3. Description of the suspension

The magnetic suspension is composed of a magnetic ground and a levitating proof mass, as represented in Fig. 1. The ground is composed of four permanent magnets oriented in the so-called '2D opposite' configuration according to [18] meaning that magnets along the diagonal have the same polarization. Multiple layers of permanent magnets (e.g. we used two layers of NdFeB magnets) with the same polarization can be added to increase the field intensity. The geometrical dimensions and material proper-ties of the magnets used to fabricate the suspension prototype are listed in Table 1 [30]. The levitating part of the suspension is

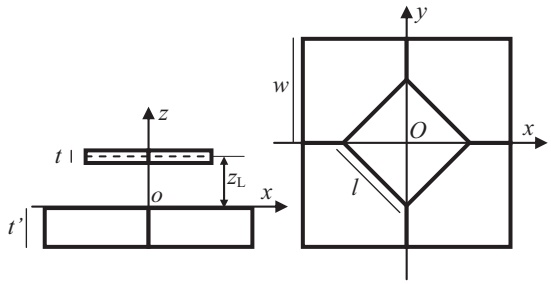

Fig. 1. Geometrical parameterized dimensions of the diamagnetic suspension.

Table 1
Geometrical dimensions and material properties of NdFeB permanent magnets.

Description	*Symbol*	*Value*	*Unit*
Side length	w	20	mm
Thickness	t'	3	mm
Number of layers	N	2	–
Coercive force	H_c	860 ÷ 995	kA/m
Relative permeability	μ_r	1.05	–
Maximum working temperature	T_{max}	80	°C

Table 2
Geometrical dimensions and material properties [27] of the pyrolytic graphite levitating mass.

Description	*Symbol*	*Value*	*Unit*
Side length	l	9-10-11-12-13-14	mm
Thickness	t	1	mm
Density	ρ	2200	kg/m^3
Hor. susceptibility	$\chi_{x,y}$	-85×10^{-6}	–
Vert. susceptibility	χ_z	-450×10^{-6}	–

obtained with a square pyrolytic graphite proof mass with the properties listed in Table 2.

4. Finite elements model

The finite elements modeling starts from the discretized distribution of the magnetic field that was previously calculated with the commercial software Ansys. The magnetic field intensity calculated at a specific height is then used to compute the magnetic force induced in the diamagnetic material; this is possible through the numerical modeling of the proof mass according to the procedure proposed in this study. Firstly, the diamagnetic force acting on the graphite is calculated at an arbitrary levitation height of the proof mass; then the levitation coordinate is varied iteratively till when the equilibrium between magnetic force and gravity force is verified.

4.1. Magnetic field distribution

The distribution of the magnetic field generated by the permanent magnets is calculated by means of a 3D FEM simulation using the commercial tool Ansys 12.0. The elements *solid96* are used to model the magnets and the above air blocks; the mesh size is set to 0.5 mm and the coercive force (i.e. the measure of the magnetization as expressed by the external magnetic field strength necessary to demagnetize it) of NdFeB magnets $H_c = \pm 900$ kA/m simulates the opposite polarization. In the surrounding region, the magnetic

relative permeability of air (μ_r=1) is imposed. The first magnetization curve describing the relation between the magnetic flux density $\vec{B}$ and the magnetic field $\vec{H}$ has been obtained from the properties of the NdFeB material and imposed as a constraint in the elements simulating the magnets. The first magnetization curve is reported in Fig. 2.

Fig. 3 shows the values of the external magnetic field, arbitrarily taken at the vertical position $z=-6$ mm (see the reference system reported in Fig. 1), obtained in our FEM simulations varying the mesh size; there is not an evident variation of the external magnetic field decreasing the mesh size below 0.5 mm so increasing the number of the elements, while the computational time changes a lot. As a consequence the 0.5 mm mesh ($\approx 10^5$ elements) was considered as a good compromise to be used in the FEM simulations.

The numerical model used to calculate the magnetic field distribution only includes the magnets and the surrounding air; theoretically, the presence of the diamagnetic material in the space region above the magnets may influence the magnetic field distribution due to its permeability. However, considering that the diamagnetic permeability of the graphite is very close to that of air (μ_r=1) the missing of the levitating mass in the simulation does not introduce appreciable errors in the estimation of the magnetic field distribution. The FEM model including permanent magnets and the above air is represented in Fig. 4; the calculation results in terms of magnetic field components distribution are reported in Fig. 5. The values of the magnetic field distribution are in good agreement with the experimental measurements reported in [31].

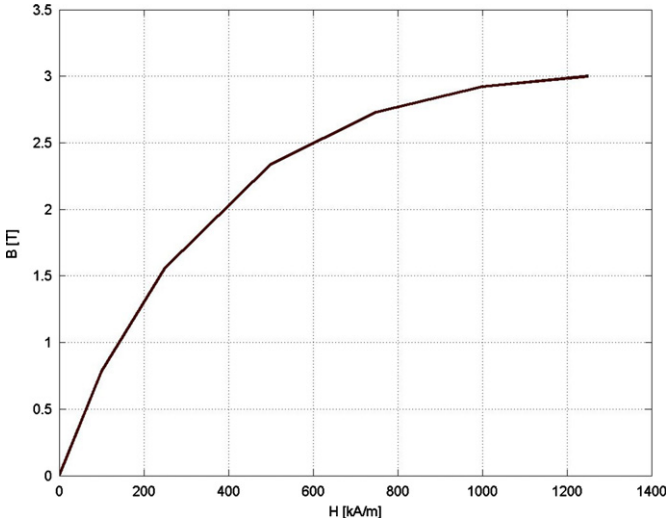

Fig. 2. First magnetization curve of the sinterized NdFeB permanent magnets.

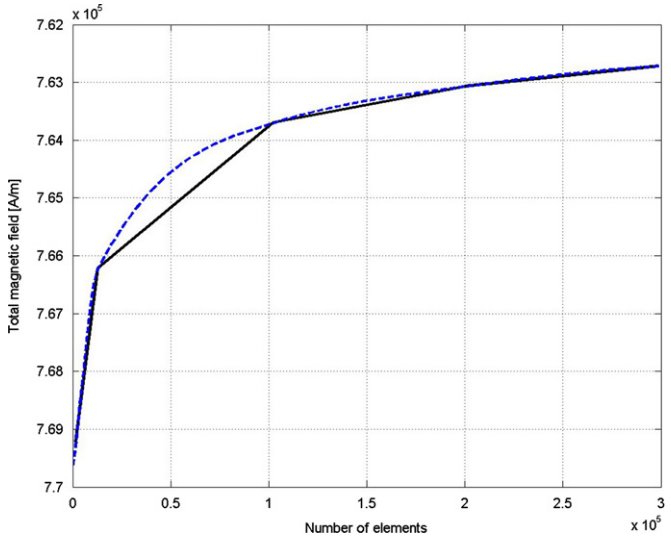

Fig. 3. Convergence graph (continuous line) and corresponding interpolation curve (dashed line) used to verify the mesh size selection for the calculus of the external magnetic field in the FEM simulation.

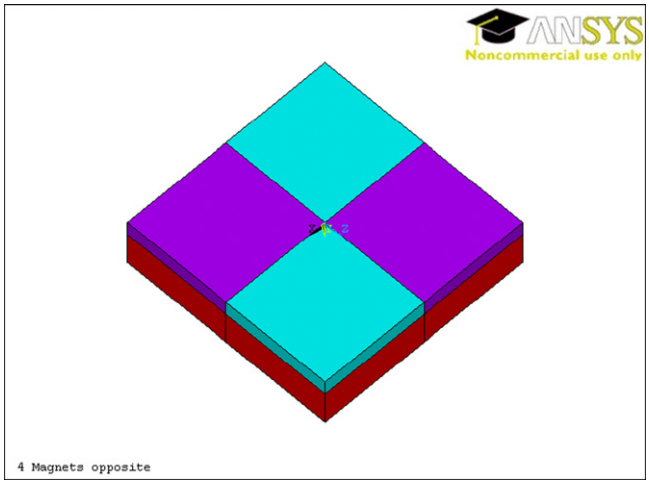

Fig. 4. Upside-down FEM model showing the 2D opposite configuration of the magnets and the above air region (red). (For interpretation of the references to color in this figure legend, the reader is referred to the web version of this article.)

4.2. Levitating mass modeling

The diamagnetic mass is discretized by dividing its volume in small elements. Due to the geometrical symmetry of the suspension, only one-half proof mass is considered, that is represented by a triangular shell with thickness t as reported in Fig. 6a. This half part of the proof mass is discretized in some portions (see Fig. 6a) and every portion, having a height equal to the double of the mesh size, is then divided in several elements, as it is reported in Fig. 6b.

Every portion of the proof mass represented in Fig. 6a i s identified by its central plane, represented with dashed lines and identified by numbers from 1 to 10. Fig. 6b reports one of the portions split up into elements; three rows of nodes are then positioned on the central plane of every mass portion, as reported in Fig. 6c. This discretizing strategy allows defining some cubic elements in every mass portion. The elements include one node at the center and two nodes on the upper and lower sides. The described distribution of nodes is suitable for the application of the finite difference method to calculate the diamagnetic force acting on each element, as described in the following. The same mesh size used for the modeling of magnetic field distribution (0.5 mm) is adopted in the levitating mass discretization.

4.3. Analysis of magnetic field symmetries

The hypothesis of symmetry at the basis of the finite element model of the suspension must be verified by analyzing the distribution of the magnetic field components in the region above magnets in addition to the symmetry of the geometry. The three components of H, calculated with the commercial software in the nodes corresponding to the arbitrarily chosen coordinate

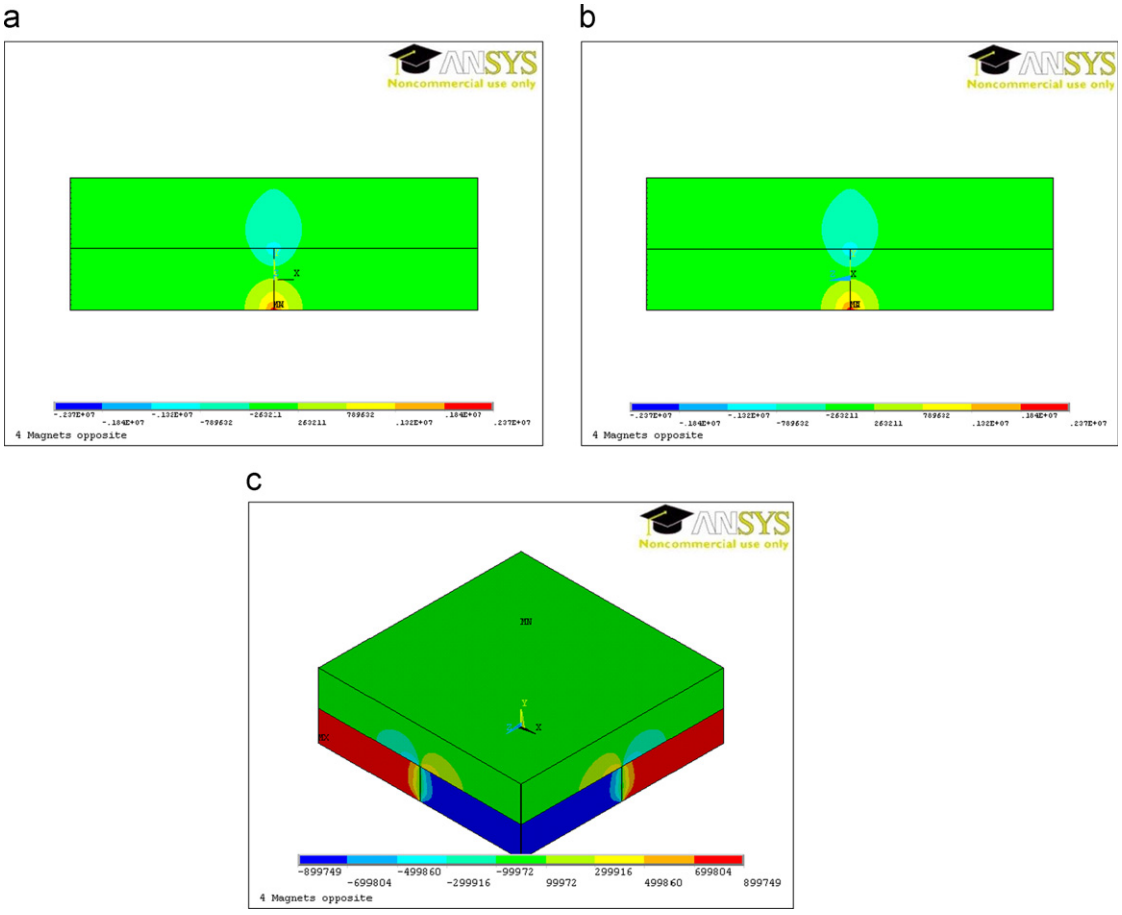

Fig. 5. Magnetic field distribution in horizontal directions (a, b) and vertical direction (c).

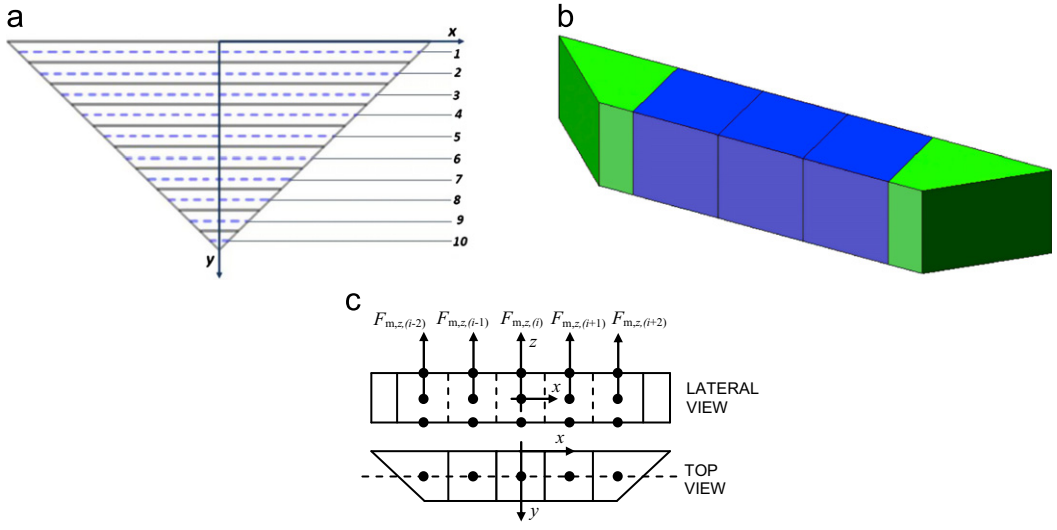

Fig. 6. Discretization approach of the diamagnetic proof mass: only half volume is considered for the symmetry of the suspension. Firstly, the mass is divided in several portions, each one identified by the central plane represented by the dashed lines in the top view (a). The elements have cubic shape except those at the end of each portion, which have trapezoidal shape (b). Every portion includes three rows of nodes situated on the symmetry plane visible in the top view (c). The nodes of the FEM model correspond to the center point of each cubic element shown in the top view; here the external magnetic field calculated by the FEM simulation is imposed for evaluating the magnetic force.

z=1 mm, are reported in Fig. 7 as an example. The results show that, due to the opposite configuration of permanent magnets, the distributions of H_x and H_y are simply rotated by a 90° angle. Instead, the distribution of H_z is equal in both x and y directions. These simple considerations lead to define the following symmetries of the magnetic field distribution in this typology of suspension:

$$H_x(x) = H_y(y) \rightarrow H_x^2(x) = H_y^2(y)$$
$$H_x(y) = H_y(x) \rightarrow H_x^2(y) = H_y^2(x)$$
$$H_z^2(x) = H_z^2(y) \quad (8)$$

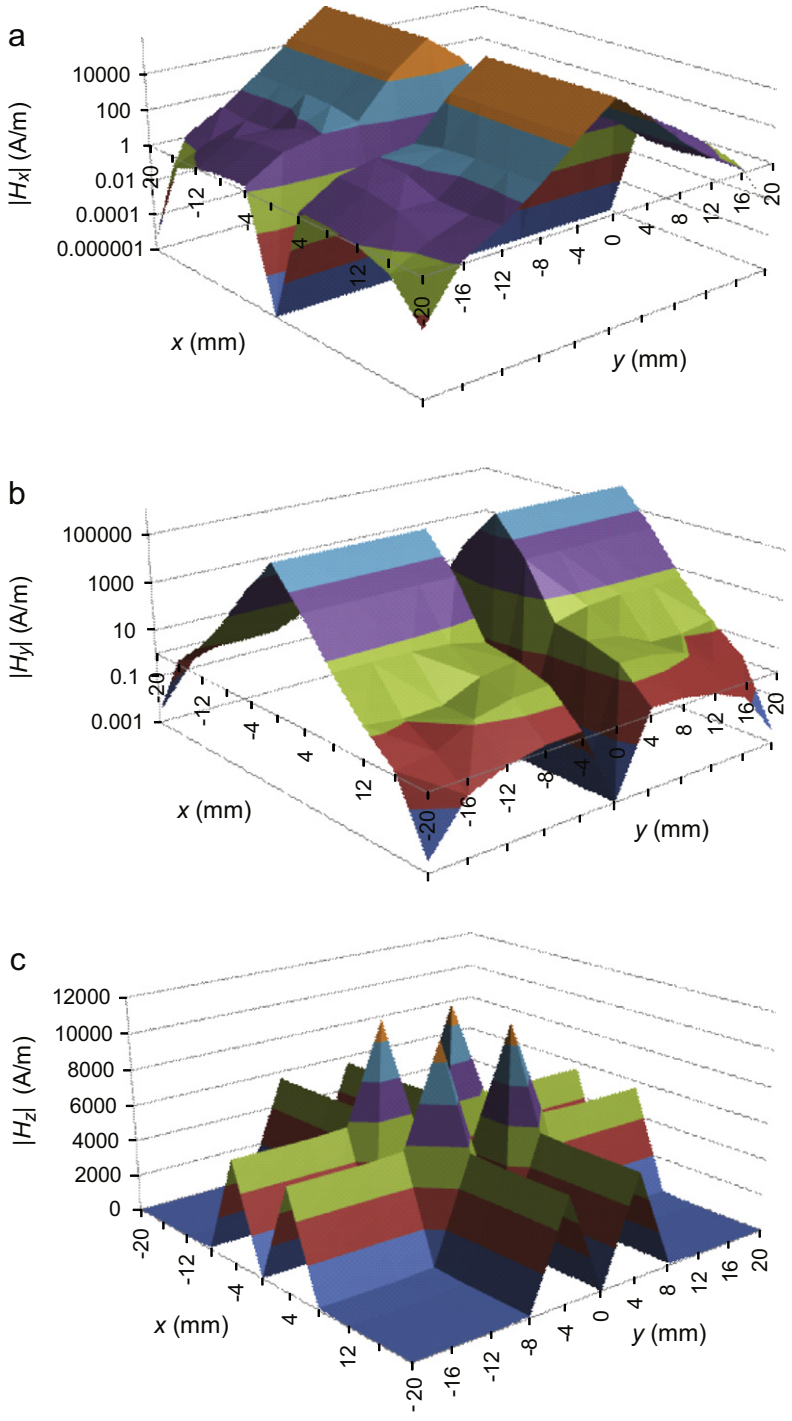

Fig. 7. Magnetic field distribution calculated by FEM software at the height $z=1$ mm.

According to Eqs. (7) and (8), the vertical magnetic force $F_{m,z}$ varies in x and y directions with the following proportionality:

$$F_{m,z}(x) \propto \frac{d}{dz}\left[\chi_x B_x^2(x) + \chi_y B_y^2(x) + \chi_z B_z^2(x)\right] \tag{9}$$

$$F_{m,z}(y) \propto \frac{d}{dz}\left[\chi_x B_x^2(y) + \chi_y B_y^2(y) + \chi_z B_z^2(y)\right] \tag{10}$$

The relation between $\vec{H}$ and $\vec{B}$ expressed by Eq. (2) indicates that the same symmetrical properties are also verified in its discretized volume. Considering that the magnetic susceptibility has the same value along the two horizontal directions (i.e., $\chi_x = \chi_y$), it is

$$F_{m,z}(x) = F_{m,z}(y) \tag{11}$$

Due to the symmetries of the magnetic field and magnetic flux density, the levitating force can be effectively calculated on the half portion of the graphite mass as described in Section 4.2. I n Fig. 7c the vertical component of the magnetic field distribution shows a magnetic potential well whose shape gives important information about the levitation stability. The position of the diamagnetic sample with respect to the potential makes it

possible to understand if the equilibrium is stable or not; the pyrolytic graphite mass, levitating over a layer of permanent magnets, is stable whenever its borders are aligned to the ones of a space portion having a magnetic potential with an upwards concavity as in case of Fig. 7c; this alignment is possible thanks to the natural 45 degrees orientation of the pyrolytic plate.

4.4. Levitating height prediction

The nodes of the mesh identifying the diamagnetic levitating mass have been defined with the approach described before for the volume discretization. With reference to the central plane of each mass portion (Fig. 6a), the coordinates of the nodes reported in Table 3 can be calculated.

For example, the central plane 4 includes three rows of nodes with 27 nodes each; the x coordinates are spaced by a value corresponding to the mesh size (0.5 mm).

The diamagnetic force acting on the proof mass is given by Eq. (7) in case of continuum domains. The same equation can be used to run the numerical model with the meshing strategy previously described; in this case, arbitrarily calling g^* the expression $\chi_x \cdot B^2{}_x + \chi_y \cdot B^2{}_y + \chi_z \cdot B^2{}_z$, its derivative with respect to the vertical direction can be calculated by means of the centered finite difference method (see Fig. 8) and is given by the following equation:

$$\frac{dg^*(i,j,k)}{dz} = \frac{g^*(i,j,k+1) - g^*(i,j,k-1)}{2\Delta z} \tag{12}$$

where i, j, k are the direction vectors for x, y, z axes respectively and Δz is the mesh size in z direction.

According to Eqs. (7) and (12), the magnetic force acting on the levitating mass is given by

$$F_{m,z} = 2\frac{1}{2\mu_0}\sum_j \left\{ \sum_{i=1}^{(n-1)/2} \sum_k \left[\frac{g^*(i,j,k+1) - g^*(i,j,k-1)}{2\Delta z} \overline{V}_i \right] \right\} \tag{13}$$

Table 3
Coordinates of the nodes of every mass portion as reported in Fig. 6. The mesh size considered for the discretization of the mass is 0.5 mm.

Central plane (j)	*Number of nodes per row (n)*	*x [mm]*	*y [mm]*	*z [mm]*
1	39	−9.5 ÷ 9.5	0.5	1.0-1.5-2.0
2	35	−8.5 ÷ 8.5	1.5	
3	31	−7.5 ÷ 7.5	2.5	
4	27	−6.5 ÷ 6.5	3.5	
5	23	−5.5 ÷ 5.5	4.5	
6	19	−4.5 ÷ 4.5	5.5	
7	15	−3.5 ÷ 3.5	6.5	
8	11	−2.5 ÷ 2.5	7.5	
9	7	−1.5 ÷ 1.5	8.5	
10	3	−0.5 ÷ 0.5	9.5	

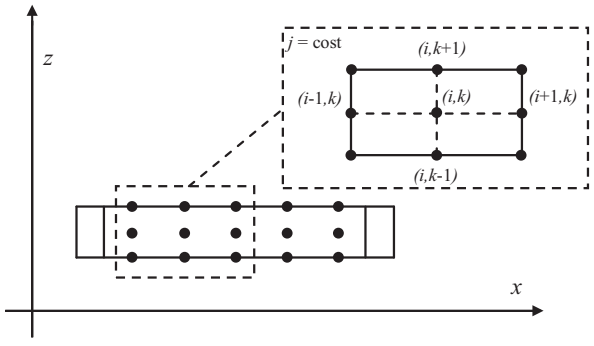

Fig. 8. Centered finite difference method applied to the discretized levitating mass.

The magnetic forces acting on the nodes are represented in Fig. 6c. The symbol V_i refers to the volume of the elements centered in the node i,k of the portion j. In case of cubic elements, it is $V_i = V_i$, instead the first and the last volumes of the portion have trapezoidal shape and their volume is $V_i = \overline{V}_{\text{out}}$ (see Table 4 for a better explanation of the volumes). The coefficient 2 at the beginning of Eq. (13) is due to the initial symmetry hypothesis.

5. Experimental setup

Some prototypes of the suspension have been fabricated and used to validate the results predicted by the numerical model in the static field through experimental measurements. The magnetic ground of the suspension is obtained with rare-earth permanent magnets made of sintered NdFeB, characterized by high values of magnetization. The magnets have been previously treated with NiCuNi surface coating to prevent corrosion. The geometrical dimensions and material properties of the magnets used in the prototypes are listed in Table 1 [30]. The properties of the levitating graphite proof mass are listed in Table 2. Some dimensional parameters are varied through the prototypes in order to characterize different configurations of the suspension. Fig. 9 shows a lateral view of one of the samples.

The layers of permanent magnets can be increased in number to enhance the magnetic field and to allow levitating heavier proof masses; the geometry of the suspension is defined through some independent parameters that can be varied to modify its static configuration and properties. The levitation height and the suspension stability (i.e. the propensity to keep the proof mass centered in the xy plane) are strongly dependent to the relative size of permanent magnets and levitating mass. It was observed that weak magnetic fields reduce the stability, as well as heavy proof masses.

The instrumentation used to characterize the suspension includes a DC voltage generator and two LK-G82 KEYENCE laser sensors (50 kHz sampling frequency, 0.2 μm ± 0.05% accuracy) with a LK-G signal controller. The measurements have been conducted on a seismic table to reduce the effects of external noise on the experimental results. A metallic supporting frame is used to align and hold the instruments. The laser sensors (see Fig. 10) are supplied by the DC voltage generator and are used to measure the static configuration of the suspension. The measured data are sent to a signal controller and then to a PC for the post-processing.

The experimental setup was conceived to study the static and the dynamic behavior of the suspension, as well as its stiffness, only in the vertical direction. This configuration is suitable for single degree of freedom devices where the mass motion is guided by lateral constraints and limited by mechanical dimples. Then, lateral motion and lateral suspension stiffness, which require dedicated simulation hypotheses and different physical explanation, are not included in this study.

6. Results

6.1. Numerical results

The magnetic force acting on the proof mass is calculated by using the described model for three tentative levitation heights of the graphite mass. The position is changed iteratively until the value of the magnetic force ($F_{m,z}$) equals the gravity force (F_g) on the levitating mass. The first tentative calculation is performed at the height $z = 1$ mm, the second iteration at $z = 2$ mm and the last third iteration at $z = 1.5$ mm.

Table 4
Summary of the modeling steps and definition of parameters and equations.

Step	Parameter	Description	Value	Unit
Data input	l	Diamagnetic mass side length	$9 \div 14$	mm
	ρ	Pyrolytic graphite density	2200	kg/m^3
	t	Diamagnetic mass thickness	1	mm
	$\chi_{x,y}$	Magnetic susceptibility in x/y directions	-85×10^{-6}	/
	χ_z	Magnetic susceptibility in z direction	-450×10^{-6}	/
	μ_0	Magnetic permeability of vacuum	$4\pi \times 10^{-7}$	N/A^2
	$H_x(i,j,k)$	Magnetic field in x direction	Preliminary FEM simulation	A/m
	$H_y(i,j,k)$	Magnetic field in y direction	Preliminary FEM simulation	A/m
	$H_z(i,j,k)$	Magnetic field in z direction	Preliminary FEM simulation	A/m
	Δ	Mesh size	0.5	mm
Computing of suspension parameters	M	Diamagnetic mass	$\rho t l^2$	kg
	P	Diamagnetic material weight force	$9.81M$	N
	y_1	Vertical position of the three rows of nodes for the calculus of the magnetic field over the magnetic layers	$z_G-\Delta$	mm
	y_2		z_G	mm
	y_3		$z_G+\Delta$	mm
	d	Diamagnetic mass diagonal	$l2^{1/2}$	mm
	a	/	$d/2$	mm
	b	Rounding of "a" to its nearest integer	Round(a)	mm
	V_i	Volume of i-th cubic element	$8\Delta^3$	mm^3
For j from 1 to $b/(2\Delta)$ in steps of 1 For w from Δ to $b-\Delta$ in steps of 2Δ				
	L_j	Length of the j-th row	$2(b-w)$	mm
	$n_{j,\mathrm{tot}}$	Number of total nodes in the j-th row	$(L_j/\Delta)+1$	/
Computing of j-w-dependent parameters	n_j	Number of nodes to be considered in the j-th row	$(n_{j,\mathrm{tot}}-1)/2$	/
	A_j	Area of the j-th portion	$2\Delta L_j$	mm^2
	V_{out}	Volume of each i-th external element	$\Delta[A_j-2\Delta^2(n_{j,\mathrm{tot}}-5)]$	mm^3
For k from 1 to 3 in steps of 1 For i from 1 to $n_{j,\mathrm{tot}}$ in steps of 1				
Construction of magnetic flux density matrices	$B_x(i,j,k)$	Magnetic flux density in x direction	$\mu_0(1+\chi_{x,y})\cdot H_x(i,j,k)$	T
	$B_y(i,j,k)$	Magnetic flux density in y direction	$\mu_0(1+\chi_{x,y})\cdot H_y(i,j,k)$	T
	$B_z(i,j,k)$	Magnetic flux density in z direction	$\mu_0(1+\chi_z)\cdot H_z(i,j,k)$	T
Computing of nodal magnetic forces	$F(i,j,1)$	Zero vector to be updated	zeros$(1,n_{j,\mathrm{tot}})$	N/m^3
	$F_{m,ij}(i,j,1)$	zero vector to be updated	zeros$(1,n_{j,\mathrm{tot}})$	N
	For c from 2 to $(n_{j,\mathrm{tot}}-1)$ in steps of 2			
	$F(c,j,1)$	Nodal magnetic force per unit volume	$[g^*(c,j,3)-g^*(c,j,1)]/(4\Delta\mu_0)$	N/m^3
	$F_{\mathrm{m},ij}(c,j,1)$	Nodal magnetic forces in cubic elements	$F(c,j,1)V_i$	N
	$F_{\mathrm{m},ij}(2,j,1)$	Nodal magnetic forces in trapezoidal elements	$F(2,j,1)V_{\mathrm{out}}$	N
	$F_{\mathrm{m},ij}(n_{j,\mathrm{tot}}-1,j,1)$		$F(n_{j,\mathrm{tot}}-1,j,1)V_{\mathrm{out}}$	N
Computing of total magnetic force	$F_{m,j}(1,j,1)$	Magnetic force in the j-th portion	$\sum_{i=1}^{n_{j,\mathrm{tot}}} F_m(i,j,1)$	N
	$F_{m,z}$	Total magnetic force	$2\sum_{j=1}^{b/2\Delta} F_{m,j}(1,j,1)$	N
	R	Magnetic force/weight ratio	$F_{m,z}/P$	/

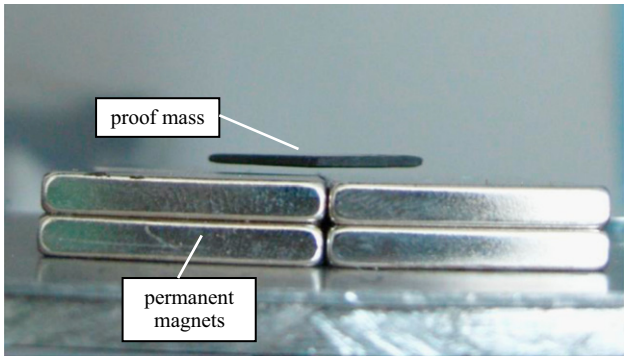

Fig. 9. Diamagnetic suspension sample used in experimental characterization of static configuration.

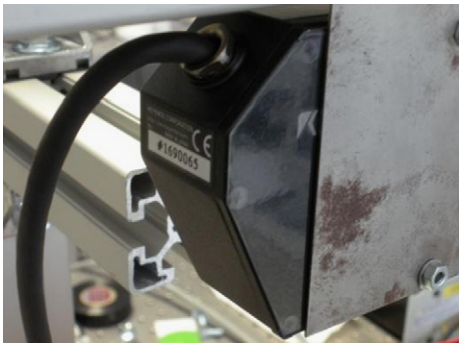

Fig. 10. Experimental equipment: laser sensor.

The total magnetic force acting on the proof mass is calculated for the three vertical positions and the ratio $R=F_{m,z}/F_g$ is obtained; the results are reported in Table 5 while the steps for the definition of the parameters and of the equations in the numerical model are summarized in Table 4. Table 4 is divided into six parts; the first part contains all the parameters used as Ansys simulation data input and the ones obtained as results in the simulation and used to calculate the diamagnetic force acting on the pyrolytic sample mass; the second part deals with the calculus of the main parameters related to the levitating sample geometry. The third part summarizes the equations relative to the nodes virtually located on each of the central planes belonging

to the portions the diamagnetic sample is divided in; these equations, omitted in the text not to create a too heavy mathematical treatment overtaking the physical purpose of this paper, were simply used to find out in the Ansys model the correct position of the nodes where to read the values of the external magnetic field acting on them. The fourth part contains the formulas for the calculus of the magnetic flux density and for the construction of the matrices whose elements are used to compute the vertical magnetic force as it is shown in the fifth and in the sixth part of Table 4.

Table 5
Values of the magnetic force predicted by the model and compared to the gravity force at three tentative levitation heights of the proof mass for different dimensions of the graphite side length.

Side length (l) [mm]	*Gravity force* (F_g) [mN]	$F_{m,z}$ [mN]		
		z=1 mm	z=1.5 mm	z=2 mm
9	1.82	3.7	1.7	0.6
10	1.97	4.5	2.2	0.8
11	2.77	5.4	2.7	1.0
12	2.89	6.3	3.2	1.2
13	3.58	7.1	3.7	1.4
14	4.44	7.9	4.3	1.6

The levitation height (z_L) is defined as the distance between the upper surface of the permanent magnets and the center of gravity of the diamagnetic mass. The levitation height corre-sponds to the vertical coordinate at which the numerical model gives the ratio R closer to the unity. This is verified, in the three cases considered, at the levitation height z_L=1.5 mm. Fig. 11 reports the value of the ratio R with respect to the vertical coordinate for different sizes of the graphite. The experimental levitation height (corresponding to R=1) is also indicated.

The numerical predicted values of R can be interpolated by the function

$$R = \frac{1}{az^3 + bz} \tag{14}$$

where the coefficients a and b have been calculated for each size of the proof mass and listed in Table 6. The fitting curves are reported in Fig. 11 as dashed lines.

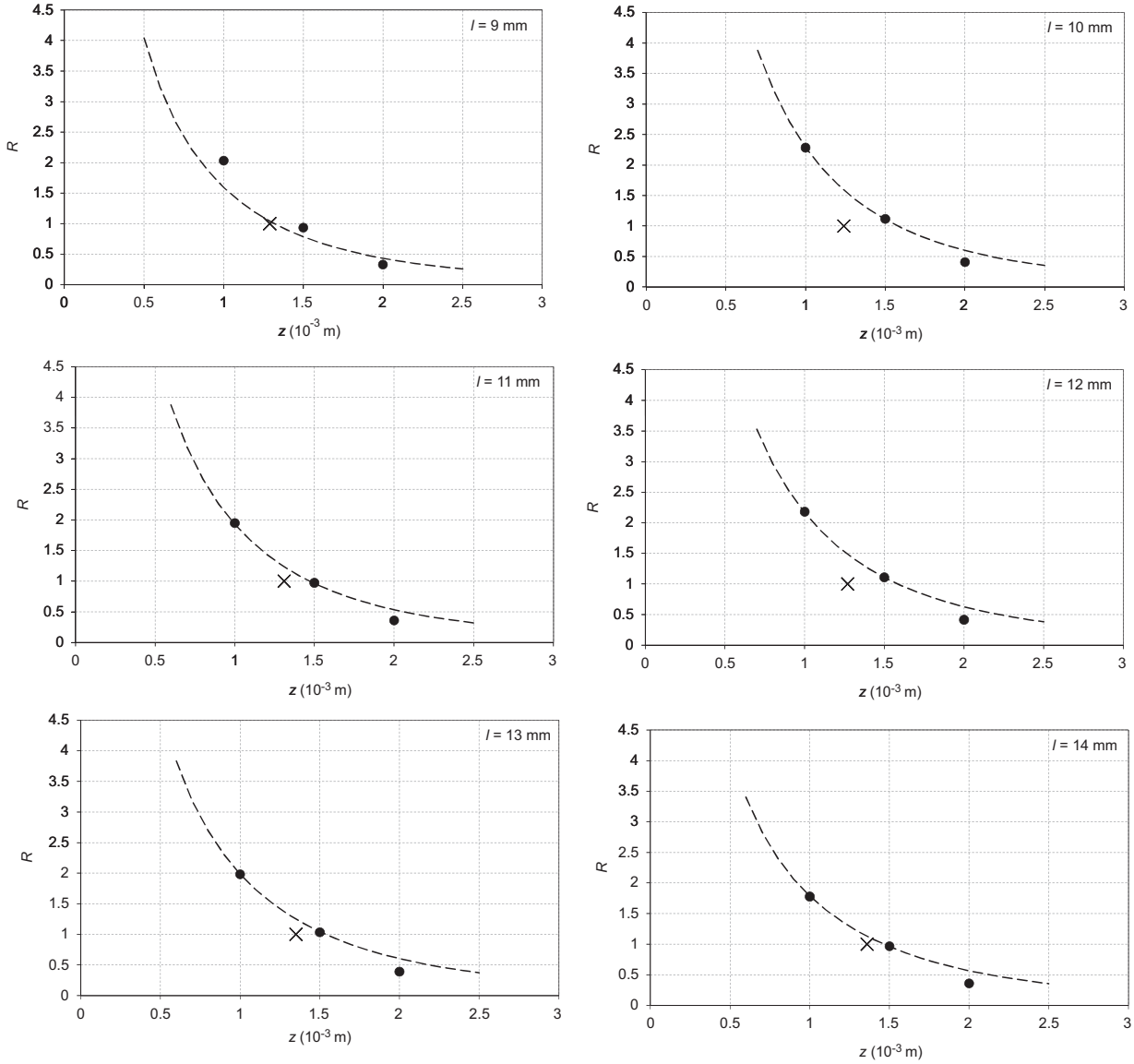

Fig. 11. Vertical forces ratio R at different vertical positions: numerical prediction (black dots) with fitting curve and experimental value (black cross) for different graphite side lengths.

Table 6
Values of coefficients a and b for different sizes of the proof mass.

Side length (l) [mm]	a [1/m^3]	b [1/m]
9	1.77×10^8	3.16×10^2
10	1.33×10^8	3.03×10^2
11	1.38×10^8	3.80×10^2
12	1.12×10^8	3.50×10^2
13	1.08×10^8	3.96×10^2
14	1.08×10^8	4.51×10^2

Table 7
Comparison between numerical and experimental values of levitation height and magnetic stiffness.

Side length (l) [mm]	*Levitation height* (z_L) [mm]	*Experimental levitation height* ($z_{L,\mathrm{exp}}$) [mm]	*Magnetic stiffness* (k_m) [N/m]	*Experimental magnetic stiffness* ($k_{m,\mathrm{exp}}$) [N/m]	*Experimental dynamic magnetic stiffness* ($k_{md,\mathrm{exp}}$) [N/m]
9	1.45	1.29	2.62	3.55	2.18
10	1.58	1.24	2.55	4.58	2.25
11	1.47	1.31	3.53	4.60	3.01
12	1.59	1.27	3.46	5.70	2.99
13	1.54	1.35	4.15	5.50	3.53
14	1.47	1.36	5.09	5.96	4.15

The magnetic stiffness of the suspension can be obtained from the derivative of the magnetic force at the equilibrium position:

$$k_m = -\frac{dF_{m,z}(z=z_L)}{dz} \tag{15}$$

that, considering the definition of R becomes

$$k_m = -\frac{d[F_g \cdot R(z=z_L)]}{dz} = -mg\frac{dR(z=z_L)}{dz} \tag{16}$$

From Eqs. (14) and (16) it results finally

$$k_m = mg\frac{3az_L^2+b}{(az_L^3+bz_L)^2} \tag{17}$$

The curve fitting numerical results have been calculated for every configuration of the suspension. The levitation height (z_L) and the suspension stiffness (k_m) resulting from the simulations have been obtained from the fitting curve in correspondence to R=1; these values are reported respectively in the second and fourth columns of the next Table 7.

6.2. Experimental results

Firstly, the static equilibrium position of the suspension depending to the dimensions of its parts has been characterized. The suspension reaches its static equilibrium position at the vertical coordinate where the diamagnetic force acting on the proof mass equals its gravity force; this coordinate gives the static levitation height of the suspension ($z_{L,\mathrm{exp}}$). The gravity force (F_g) is constant for a given size of the levitating mass and the diamagnetic force ($F_{m,z}$) can be easily calculated at the equilibrium position (corresponding to $z_{L,\mathrm{exp}}$).

The laser sensor is used to measure the distance between the magnets surface and the upper surface of the proof mass, which is situated at the coordinate z_{surf}. Then the thickness (t) of each proof mass is measured as the average value of 9 detections taken in different points of every graphite mass. From the comparison of all the measurements of thickness, the average variance 1.707×10^{-3} has been found. Finally, the experimental levitation height value is calculated as

$$z_{L,\mathrm{exp}} = z_{surf} - \frac{t}{2} \tag{18}$$

At the equilibrium position, the diamagnetic force is simply expressed by

$$\vec{F}_{m,z}(z=z_{L,\mathrm{exp}}) = \vec{F}_g = \rho V g, \tag{19}$$

where V is the volume of the proof mass and g is the acceleration of gravity.

The static levitation height was measured in presence of N=2 layers of permanent magnets and different graphite masses having variable side lengths and thickness t=1 mm. The measurements results are reported in Fig. 12 and listed in Table 7 (third column).

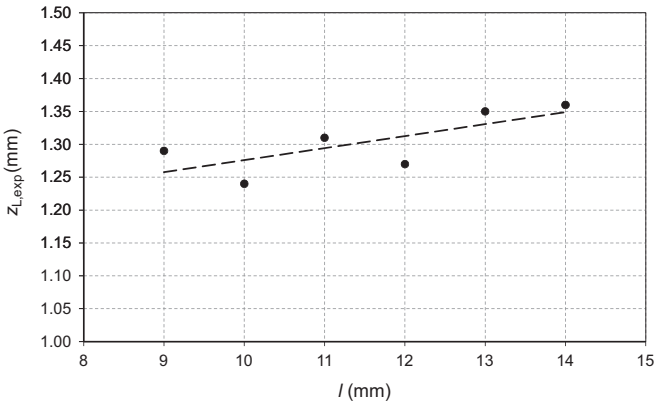

Fig. 12. Experimental levitation height with graphite thickness t=1 mm and variable side lengths in presence of N=2 layers of permanent magnets.

The results reported in Fig. 12 show a linear relation between the graphite side length and the levitation height in the range considered. The levitation height increasing testifies that the additional diamagnetic material determines the additional contribution $\Delta\vec{F}_{m,z}$ to the magnetic force, which is larger than the additional gravity force $\Delta\vec{F}_g$ due to the proof mass widening. This effect can be explained by considering that the magnetic field generated inside the graphite is opposite in direction to the field generated by permanent magnets; the entity of the induced field is proportional to the volume of the proof mass. These considerations are limited to the range of graphite side values considered in the experiments.

6.3. Comparison of results

The levitation height predicted by the numerical model (z_L) and measured by experiments ($z_{L,\mathrm{exp}}$) is reported in Table 7 for different graphite side lengths.

The magnetic stiffness (k_m) predicted by the numerical model with Eq. (17) is also reported in Table 7. These values are compared with the experimental magnetic stiffness ($k_{m,\mathrm{exp}}$), obtained as the derivative of the fitting curve reported in Fig. 11 at the coordinate $z_{L,\mathrm{exp}}$ for every configuration of the suspension. Additionally, the dynamic stiffness of the suspension ($k_{md,\mathrm{exp}}$) i s also reported in Table 7; it has been calculated from the experi-mental measurement of the resonance frequency by means of the relation $k_{md,\mathrm{exp}} = m\omega_n{}^2$ where ω_n is the angular frequency at resonance of a mass-spring system whose damping effect is neglected. A mechanical shaker, controlled by a sinusoidal func-tion generator, was used to simulate vibrations coming from external sources.

The dynamic stiffness (see Table 7) is less than the static one determined by means of the fem simulation and this is due to the

magneto-mechanical system non-linearity and to the fact that the fem approach overestimates the real values of the stiffness of the system.

7. Conclusions

This study introduces a strategy for the numerical modeling of a magnetic suspension based on the diamagnetic levitation principle. The approach proposed starts from the preliminary discretization of the space region interested by the magnetic field distribution; the magnetic force acting on the diamagnetic mass and producing levitation is calculated in correspondence to the nodes of the mesh. Finally the static levitation height of the suspension is determined by an iterative procedure till when the equilibrium condition between magnetic and gravity force is verified. The accuracy of the result depends on the mesh size; the final results have been interpolated by a fitting curve to predict the levitation height. The numerical calculations have been verified by means of experimental measurements of the levitation height in different dimensional configurations of the suspension.

The results show a good agreement between numerical predictions of the finite elements model and the experiments; the small differences are probably due to the uncertainties in magnetic properties of magnets and diamagnetic materials and to the effect of surface coating of magnets. The mesh size used in the current modeling is quite large to simplify the formalisms; however the same simulation strategy is suitable for accurate discretization of the involved domains.

References

[1] Mann BP, Sims ND. Energy harvesting from the nonlinear oscillations of magnetic levitation. J Sound Vib 2009;319:515–30.
[2] Pigot C, Delinchant B, Reyne G. Optimization of a 3D micro-accelerometer based on diamagnetic levitation. Proc OIPE 2008 Ilmenau, Germany. p. 194–5.
[3] Profijt HB, Pigot C, Reyne G, Grechishkin RM, Cugat O. Stable diamagnetic self-levitation of a micro-magnet by improvement of its magnetic gradients. J Magn Magn Mater 2009;321:259–62.
[4] Ghodsi M, Ueno T, Teshima H, Hirano H, Higuchi T. Numerical modeling of iron joke levitation using the pinning effect of high-temperature superconductors. IEEE Trans Magn 2007;43:2001–8.
[5] Miyoshi K, Shimizu H, Meguro SI, Uetake H, Hirota N, Kitazawa K. Development of compact magnet for high magnetic force. IEEE Trans Appl Supercon 2002;12:933–6.
[6] De Pasquale G, Siyambalapitiya C, Somà A, Wang J. Performances improvement of MEMS sensors and energy scavengers by diamagnetic levitation. Proc ICEAA 2009:465–8.
[7] Earnshaw S. On the nature of the molecular forces which regulate the constitution of the luminiferous ether. Trans Camb Phil Soc 1842;7:97–112.
[8] Berry MV, Geim AK. Of flying frogs and levitrons. Eur J Phys 1997;18:307–13.
[9] Geim AK, Simon MD, Boamfa MI, Heflinger LO. Magnet levitation at your fingertips. Nature 1999;400:323–4.
[10] Simon MD, Geim AK. Diamagnetic levitation: flying frogs and floating magnets. J Appl Phys 2000;87:6200–4.
[11] Boukallel M, Abadie J, Piat E. Levitated micro-nano force sensor using diamagnetic materials. Proc ICRA 2003;3:3219–24.
[12] Simon MD, Heflinger LO, Ridgway SL. Spin stabilized magnetic levitation. Am J Phys 1997;65:286–92.
[13] Simon MD, Heflinger LO, Geim AK. Diamagnetically stabilized magnet levitation. Am J Phys 2001;69:702–13.
[14] Cansiz A, Hull JR. Stable load-carrying and rotational loss characteristics of diamagnetic bearings. IEEE Trans Magn 2004;40:1636–41.
[15] Cansiz A. Static and dynamic analysis of a diamagnetic bearing system. J Appl Phys 2008;103(3):34510–4.
[16] Elbuken C, Khamesee MB, Yavuz M. Eddy current damping for magnetic levitation: downscaling from macro-to micro-levitation. J Phys D Appl Phys 2006;39:3932–8.
[17] Chen JY, Zhou JB, Meng G, Zhang WM. Evaluation of eddy-current effects on diamagnetic bearings for microsystems. IEEE Trans Ind Electron 2009;56:964–72.
[18] Barrot F. Acceleration and inclination sensors based on magnetic levitation. Application in the particular case of structural health monitoring in civil engineering. PhD thesis. EPFL Lausanne, Switzerland; 2008.
[19] Chen JY, Zhou JB, Meng G. Diamagnetic bearings for MEMS: performance and stability analysis. Mech Res Commun 2008;35:546–52.
[20] Barrot F, Sandtner J, Bleuler H. Acceleration sensor based on diamagnetic levitation. In: Proceedings of the IUTAM symposium on vibration control of nonlinear mechanisms and structures, Munich, Germany; 2005. p. 81–90.
[21] Garmire D, Choo H, Kant R, Govindjee S, Séquin CH, Muller RS, et al. Diamagnetically levitated MEMS accelerometers. In: Proceedings of the 14th transducers and eurosensors, Lyon, France; 2007. p. 1203–1206.
[22] Tang WC, Lim MG, Howe RT. Electrostatic comb drive levitation and control method. J MEMS 1992;1:170–8.
[23] Chyuan SW, Liao YS, Chen JT. Computational study of the effect of finger width and aspect ratios for the electrostatic levitating force of MEMS combdrive. J MEMS 2005;14:305–12.
[24] Li Q, Kim KS, Rydberg A. Lateral force calibration of an atomic force microscope with a diamagnetic levitation spring system. Rev Sci Instrum 2006;77:065105-1–13.
[25] Moser R, Bleuler H. Precise positioning using electrostatic glass motor with diamagnetically suspended rotor. IEEE Trans Appl Supercon 2002;12:937–9.
[26] Moser R, Barrot F, Sandtner J, Bleuler H. Optimization of two-dimensional permanent magnet arrays for diamagnetic levitation. In: Proceedings of the 17th MAGLEV, Lausanne, Switzerland; 2002.
[27] De Pasquale G, Iamoni S, Somà A. Modeling and experimental validation of levitating systems for energy harvesting applications. Proc DTIP 2011:97–102 Aix-en-Provence, France.
[28] Alqadi MK, Al-Khateeb HM, Alzoubi FY, Ayoub NY. Effects of magnet size and geometry on magnetic levitation force. Chin Phys Lett 2007;24:2664–6.
[29] Chetouani H, Delinchant B, Reyne G. Efficient modeling approach for optimization of a system based on passive diamagnetic levitation as a platform for bio-medical applications. Compel 2007;26:345–55.
[30] Pyrhönen J, Jokinen T, Hrabovcová V. Design of rotating electrical machines. John Wiley and Sons; 2009 p. 232.
[31] De Pasquale G, Siyambalapitiya C, Somà A. Experimental identification of rare-Earth magnetic suspensions for levitating systems in the micro and meso scales. Smart Struct Syst, submitted for publication.